# Mitochondrial Transcription Factor A Regulates Foxp3+ T Cell Mediated Maintenance of CD4+ T Cell Landscapes and Immunological Aging

Kai Guo[1, 2, $], Zhihan Wang[3, 4, $], Trishna Debnath[3, $], Het Mehta[3], Eden Abrham[3], Zachery Even[3], Mansib Rahman[3], Abby Lund Da Costa[3], Shilpi Jain[3], Xusheng Wang[5], Junguk Hur[2], Gopal Murugaiyan[6], Adrian T. Ting[7], Holly Brown-Borg[2], Donald A Jurivich[3], Nadeem Khan[8], Ramkumar Mathur[3, *]

1. Department of Neurology, University of Michigan, Ann Arbor, MI 48109, USA
2. Department of Biomedical Sciences, School of Medicine and Health Sciences, University of North Dakota, Grand Forks, ND 58202, USA
3. Department of Geriatrics, School of Medicine and Health Sciences, University of North Dakota, Grand Forks, ND 58202, USA
4. West China School of Basic Medical Sciences & Forensic Medicine, Sichuan University, Chengdu, Sichuan, China
5. Department of Biology, University of North Dakota, Grand Forks, ND 58202, USA
6. Ann Romney Center for Neurologic Diseases, Brigham and Women's Hospital, Boston and Harvard Medical School, Boston, MA 02115, USA
7. Department of Immunology, Mayo Clinic, Rochester, MN 55905, USA
8. Dept of Oral Biology, College of Dentistry, University of Florida, Gainesville, FL 32603, USA

[$]Authors contributed equally
*Correspondence
Ramkumar Mathur, Department of Geriatrics, School of Medicine and Health Sciences, University of North Dakota, Grand Forks, ND 58202, USA
Email: ramkumar.mathur@und.edu

**Abstract**
A decline in mitochondrial activity has been linked to T cell dysfunction and the progression of a variety of diseases. It is unclear whether the mitochondrial function in regulatory T cells (Tregs) determines effector T cell fate decisions and regulates steady-state inflammation. We show that loss of Mitochondrial Transcription Factor A in Foxp3$^+$ Tregs (TFAM cKO) affects the cellular and transcriptional dynamics of CD4$^+$ T cells, resulting in disproportional cellular heterogeneity and prevalence of pathogenic CD4$^+$ T cell subsets. Failure to modulate CD4$^+$ T cell responses results in systemic inflammation, immunological aging, and shortened lifespans in TFAM cKO mice. Furthermore, we found that TFAM heterozygous (Het) mice with 50% allelic restoration had a progressive decrease in physiological, cognitive, and neuromuscular activity starting at 8 months, implying that the TFAM Het mouse model has the potential to be used for in-depth research on age-related inflammatory diseases. Overall, TFAM depletion in Tregs explains the steady-state reduction in Treg function with age. TFAM restoration in Tregs could be a target for preserving the homeostatic CD4$^+$ T cell pool and avoiding cognitive impairments caused by inflammation induced aging (inflammaging).

**Introduction**
The immune system is constantly reshaping in response to antigenic and metabolic challenges[1,2]. Notably, Foxp3$^+$ regulatory T cells (Tregs) act as master regulators of the immune cell landscape, reorganizing effector CD4$^+$ T cell responses to create a distinct inflammation without putting the host at risk[3-6]. Dysregulation of Treg cells unleashes effector CD4$^+$ T cells, leading to amplification of the inflammatory response and concomitant tissue inflammation and autoimmunity[7-10]. Interestingly, in aging humans and animal models, a significant increase in Treg cells has been linked to an increased proportion of cytotoxic, exhausted, and effector memory T cells, with a consequent decrease in the proportion of naive CD4$^+$ T cells[6,11,12]. However, it remains unclear if a residual pool of peripheral Tregs acquires a distinct immunosuppressive repertoire during thymic degeneration in aging and, as a result, influences the functional composition of CD4$^+$ T cell subsets. A range of data from mouse models of aging shows the impact of functional impairment of Tregs in inflammation control[1,13]. The reduced expression of key mitochondrial proteins has been shown to enhance oxidative stress and cellular senescence during aging, implying a direct association of decreased mitochondrial function with cellular aging[14-16]. The Mitochondrial Transcription Factor A (TFAM) has been linked to the regulation of T-cell effector

responses[16-19]. However, there is a lack of data on whether TFAM or mitochondrial function regulates the suppressive function of Foxp3$^+$ Tregs, thereby influencing the CD4$^+$ T cell functional fates during aging. To study how Treg-specific TFAM shapes the T effector subsets and their functional phenotype, we leveraged a Foxp3-specific TFAM conditional knockout mice (Foxp3$^{Cre}$Tfam$^{f/f}$) and performed large-scale unsupervised single-cell RNA sequencing (scRNA-seq). We found that TFAM ablation results in a heterogeneous population of CD4$^+$ inflammatory effector T cells. The scRNA-seq research indicates that the plasticity of Tregs is compromised in Foxp3$^{Cre}$Tfam$^{f/f}$ mice, which results in a predominance of pathogenic effector CD4 cells that promote inflammation and age-related pathologies.

## Results

### TFAM in Foxp3$^+$ Tregs modulates CD4-lineage and regulates immune-mediated senescence.

To examine how TFAM dysfunction influences cellular homeostasis in the spleen, we conducted scRNA-seq from the whole spleens of Foxp3$^{Cre}$Tfam$^{f/f}$ (cKO) and Tfam$^{f/f}$ (WT) mice. A total of 14,198 (cKO) and 34,958 (WT) cells from spleen were obtained, and erythroid cells were excluded from subsequent analysis. Based on canonical lineage-defining markers, 21 cell types (26 clusters) were identified in both groups (Fig. 1A, B, Fig. S1A, S1B, S1C). TFAM loss in Foxp3 cells, on the other hand, led to an unrestricted inflammatory phenotype of CD4$^+$ T cells with considerable enrichment of pathways linked with TNF signaling, inflammation-induced aging, and cancer (Fig. S1D, Supplemental Table S1). While a number of aging-related genes, such as *S100a6* and *Zfp3612*, were significantly elevated, the expression of longevity-related genes (*Cd79b* and *Fcer2a*) was downregulated (Fig. S1E). To examine the impact of Treg-specific TFAM deficiency in the regulation of cellular heterogeneity and distribution of CD4$^+$ T cell subsets during a steady-state, we analyzed the heterogenicity of CD4$^+$ T cell subsets. Based on the canonical markers, we identified six distinct CD4$^+$ T cell subsets as, naïve (*Sell*, *Lef1*, *Tcf7*), T effector memory (TEM: *S100a4*, *S100a6*), exhausted T cell (*Tnfsf8*, *Tbc1d4*), normal Tregs (nTregs: *Ikzf2*, *Il2ra, Cd74*), aged Tregs (aTregs: *Icos*, *Rgs1*) and cytotoxic T cells (*Ccl5*, *Gzma*, *Gzmb*) (Fig. 1C, 1D). We subsequently evaluated the relative changes in each CD4$^+$ T cell subset in cKO versus WT mice (Fig. 1E, Fig. S2A). Surprisingly, TFAM cKO mice had a marked increase in aTregs (105.6%) and a slight decrease in nTregs (-6.4%), with a concomitant decrease in (-29.8%) and exhausted (-25.4%) T cell subsets. Furthermore, the TFAM cKO was enriched in TEM (208.4%) and cytotoxic (250.3%) T cell subsets. We then examined the age-related differentially expressed genes and molecular pathways in CD4$^+$ T cells of TFAM cKO and WT mice (Fig. 1F, Fig. S2B, Supplemental Table S2). We found that inflammatory TNF$\alpha$ signaling was predominantly enriched in TEM, exhausted, and aTregs in cKO mice. We also found increased calcium, cytokine and chemokines signaling pathways and decreased hematopoietic lineage turn over (Fig. 1F). Furthermore, IL-17 signaling was found to be more prevalent in TEM, exhausted, aTregs and nTregs populations (Fig. 1F). IL-17 enrichment has been linked to being associated with the conversion of Tregs into IL-17-producing phenotype, acting as an important determinant of Treg plasticity[20-23].

Since cellular differentiation is central to maintaining the CD4$^+$ T cell functional diversity, we utilized scRNA-seq data to identify the multilineage differentiation state and lineage relationships among these CD4$^+$ T cell clusters (Fig. 1G, Fig. S2C). Notably, we observed a differentiation trajectory with three bifurcation points indicating fate decisions and two primary differentiation paths (P1 and P2) with seven Monocle states 1-7 (Fig. 1G, Fig. S2D). Parsing the Monocle states with WT and cKO CD4$^+$ T cells on the single-cell trajectory revealed that cells from the WT mainly converged on states 4, 5, and 6, while cells from cKO converged more on states 1, 2, and 6 (Fig. 1G, Fig. S2D). We also compared the cells occupied in these different states between WT and cKO mice (Fig. S2E). We found that states 4, 5, 6 were primarily consist of the naïve T cells in both WT and cKO groups, and the naïve T cells showed increased states 1, 2 and 7 in cKO. Notably, aTregs cells were found to be mainly increased in state 1, while the cytotoxic T cells were reduced in states 1 and 7 in cKO (Fig. S2E). These findings suggested that the CD4$^+$ T cells from WT mice mainly follow a cell fate trajectory (P1), and cells from cKO cells instead had a preferred lineage bias toward state 1 (P2) (Fig. 1G). To further verify the directionality in the pseudotime trajectory, we performed RNA velocity analysis to estimate the expression of unspliced and spliced mRNAs in the trajectory (Fig. 1H). The RNA velocity analysis also showed a clear directional flow at the end of each branch point, further corroborating the Monocle analysis (Fig. 1G). However, it's also worth noting that some RNA velocity vectors do not follow specific trajectories. To reveal the sequential dynamics of gene expression along each branch, we also visualized the gene expression dynamics along the pseudotime trajectory and observed four distinct clusters according to their expression pattern (Fig. 1I). Genes in cluster 1, such as *Klf3*, *Sell*, *Bcl2*, and *Satb1*, were highly expressed in the early stages of the differentiation process. Genes in

cluster 2 such as *Anxa2*, *S100a4*, *Ccl5*, *S100a6,* and *Lgals1* were highly expressed in the terminally differentiated cells. Functional enrichment analysis of the four clusters revealed that cluster 1 was highly enriched in the hematopoietic pathway. Cluster 2 was enriched in Parkinson's disease, Amyotrophic lateral sclerosis (ALS), Alzheimer's disease, and oxidative phosphorylation pathways (Fig. 1I, Supplemental Table S3). We also examined the enriched KEGG pathways related to each state by using significantly up-regulated genes. We observed a significant increase in hematopoietic pathways essential to cell renewal and homeostasis in the P1. Interestingly, age-related diseases such as Alzheimer's disease, ALS, and Parkinson's disease showed a significant increase in state 1 (Fig. S2F, Supplemental Table S4). Notably, the homeostasis of $CD4^+$ T memory cells is more dynamic than that of naïve T cells. We detected a significant increase in the effector memory $CD4^+CD44^{hi}CD62L^{lo}$ population and a decrease in the naive $CD4^+CD44^{lo}CD62L^{hi}$ population in spleen and lymph node (LN) in cKO mice (Fig. 1J, 1K). Importantly, when cultured with WT $CD4^+$ T effector cells, Tregs from TFAM cKO mice displayed less suppressive capacity than Tregs from WT mice and led to increased $CD4^+$ T cell suppression, indicating that TFAM loss reduces Treg functional ability (Fig. 1L). Overall, our results suggest that TFAM participation in Tregs is critical for the regulation of $CD4^+$ T cell transcriptional programming. Inadequate TFAM response in Tregs shapes the cellular and transcriptional programming of $CD4^+$ T cells towards a pathologic inflammatory CD4 niche, which eventually leads to age-related Alzheimer's disease, Parkinson's disease, Amyotrophic lateral sclerosis, and malignancy.

**TFAM ablation causes systemic pathology and promotes immunological aging in $Foxp3^{Cre}Tfam^{f/f}$ mice.**
The ablation of CD4-specific TFAM has been shown to promote cellular senescence, and mice lacking CD4-specific TFAM exhibited an age-associated cellular phenotype with heightened inflammation and accelerated death[16]. TFAM expression in Tregs ($Foxp3^+$) has been shown to influence the $CD4^+$ T cell inflammatory response. Therefore, we examined cell physiology, inflammation, and survival of mice that are conditionally deleted TFAM in Tregs ($Foxp3^+$). Interestingly, pups from these mice were born with normal Mendelian ratios. However, after four weeks, cKO mice began to develop a broad range of morphological abnormalities, including hair loss, decreased body growth, splenomegaly, lymphadenopathy, signs of kyphosis on X-ray imaging, and gradually lethargic behavior with limited mobility and a considerably shorter life span ($p$ = 0.0001) (Fig. 2A-D). When compared to WT mice, cKO animals had a thymic atrophy, increased muscle devastation, reduced fat cells content in the skin, and lower bone density at 8-10 weeks of age (Fig. 2B, 2E, 2F). The physical and physiological deformities in cKO mice correlated with robust systemic inflammation in multiple organs including colon, lung, liver, and kidney (Fig. S3A). The systemic inflammation was characterized by elevated TNF$\alpha$, IL-6, IFN$\gamma$, and serum cytokines (Fig. 2G, Fig. S3B), as well as multiorgan histopathologic analysis by H&E staining (Fig. 2E). Furthermore, cKO mice demonstrated a loss of the spleen marginal zone (Fig. 2H). These data indicated that competent mitochondrial function regulated by TFAM was indispensable to maintaining the suppressive function of Tregs that eventually regulated the homeostatic steady state inflammation in the body. A loss of TFAM-induced Treg function can lead to severe tissue pathology as well as the development of an age-associated phenotype and premature death (Fig. 2D). We then employed immunohistochemistry and flow cytometry to compare the mitochondrial potential (Mitospy) of WT and TFAM cKO splenic Treg cells. We found that Mitospy was substantially higher in TFAM cKO mice, implying that TFAM cKO animals might have been more susceptible to pathogenic oxidative stress (Fig. 2H, 2I). In addition, we found that the expression of aging markers such as p16 and p21 were increased in cKO mice (Fig. 2J). Furthermore, cKO mice had significantly higher levels of CDK4, PCNA, p53, p16, and p21 at the protein level (Fig. 2K). Following that, we performed bulk RNA sequencing (RNA-seq) on whole spleens from WT and cKO animals. The RNA-seq data showed an interesting pattern of considerable overexpression of inflammation and age-related genes in cKO mice (Fig. 2L). The multiorgan Gene Set Enrichment Analysis (GSEA) analysis indicated a substantial enrichment of pathways associated with age-related physiological manifestations, such as brain neuroactive ligand-receptor pathways, diminished splenic protein export, and aberrant skin clock rhythm pathways (Fig. 2M, Supplemental Table S5). Aside from pointing to the potential of a link between TFAM and immunological dysfunction, our findings indicate a strong link between Tregs deficient in TFAM and an increase in inflammatory markers and inflammaging.

**TFAM conditional knockout mice exhibited a predominance of inflammation and cell death activation.**
Because the combined activity of transcription factors (TF) is mainly responsible for the regulation of $CD4^+$ T cell identification and function[8,24,25], we examined the specific set of regulons that appear to be active within the identified subsets. There was a total of 177 high-confidence regulons identified (Fig. 3A). The regulons including *Irf2*, *Bcl11a*, *Irf8 and Irf9* were primarily active in WT cells, whereas *Nfkb2*, *Nfatc1*, *Rora*, and *Runx2* were mainly active in cKO cells (Fig. 3A, Fig. S4). The regulons, such as *Egr1*, *Junb* and *Xbp1,* were high activity in aTregs,

exhausted T cells and nTregs in cKO mice, and *Runx3* was found to be highly active in cytotoxic T cells in cKO mice (Fig. 3A). Some regulons, such as *Ddit3, were* active among all cell types across WT and cKO (Fig. 3A). We next compared the expression of the inflammatory genes such as *Prdm1*, *Nfkb1*, *Nfkb2* and *Ahr* among all $CD4^+$ T cells between WT and cKO (Fig. 3B). All these genes were up-regulated in cKO cells, especially in Tregs cells. We also found elevated levels of systemic inflammatory cytokines such as TNF$\alpha$, IL-6 and IL-1$\beta$ responses in TFAM cKO mice (Fig. 3C). We next investigated whether the defect in $Foxp3^+$ Tregs contributes to increased inflammatory responses and promote bystander cell death pathways in these mice. Notably, scRNA-seq findings indicate a rise in the inflammatory $CD8^+$ T cell and NK cell populations, as well as the B cell population (Fig. 1A, S1B). In contrast, when comparing cKO mice to WT mice, the number of naive T cells and naive B cells significantly decreased (Fig. 1A, Fig. S1B). Increased TNF$\alpha$ responsive signaling in CD4 and B cell types is associated with TFAM dysfunction in $Foxp3^+$ Tregs (Fig. S1E). Inflammatory signals have been shown to cause a decrease in mitochondrial membrane potential as well as the onset of cell death signals[26-28]. Mitochondrial dysfunction is often associated with high levels of systemic inflammation and programmed cell death. Bulk RNA-seq results revealed that cKO animals had higher levels of genes related to programmed cell death than WT mice (Fig. 3D). Increased programmed cell death, apoptosis, and necroptosis were further confirmed with western blot by detecting cleaved caspase-3 and cleaved caspase-8, I$\kappa$B$\alpha$, and activation of RIPK1, RIPK3, and MKLK proteins phosphorylation (Fig. 3E). Increased Annexin/PI cell death was observed in the spleen and skin tissue of cKO mice, consistent with the low mitochondrial potential and inflammatory environment found in cKO mice (Fig. 3F). Compared with WT, the pathways such as Alzheimer's disease, Amyotrophic lateral sclerosis, Parkinson's disease, and Oxidative phosphorylation were highly up-regulated in monocytes, macrophages, and dendritic cells (DC) in cKO (Fig. 3G). These results provide insight into how Tregs lacking in TFAM govern inflammatory and cell death-related transcriptional factors and regulators in distinct CD4 subsets, as well as amplifying systemic inflammation and cell death in a variety of organs.

**Restoring mitochondrial activity reduces inflammation and aging pathologies.**

Next, we sought to test whether blocking oxidative stress will limit the pathological $CD4^+$ T cell subsets and mitigate successive inflammatory responses in cKO mice[29-31]. There is substantial evidence to support the use of flavonoid resveratrol (RSV) as an anti-inflammatory and antioxidant in the treatment of age-related diseases[32,33]. The pathophysiology of cKO mice was examined for four weeks by administering resveratrol to them at a dose of 7 mg/kg every other day (Fig. 4A). Intriguingly, RSV treatment reduced skin mitochondrial membrane potential, and protected mice against histological damage including lung, liver, and kidney (Fig. 4B, Fig. S5A). TNF$\alpha$ and IL-6 levels were significantly reduced in RSV-treated mice compared to untreated animals (Fig. 4C, 4D). In addition, RSV therapy reduced the expression of age-related p16 and p21 gene expression detected in splenocytes (Fig. 4E, 4F). Together, RSV treatment appears to decrease systemic inflammation and ameliorate pathological and immunologic aging. However, more extensive study on senolytics is needed to explain the molecular pathways involved in restoring Treg function. Because complete TFAM deletion in $Foxp3^{Cre}$ Tregs promotes immunological aging and shortens longevity, it is difficult to study age-related disorders in mice with a complete deletion of TFAM in Tregs. Therefore, we used mice with a partial ablation of TFAM (TFAM Het) in Tregs ($Foxp3^{Cre}TFAM^{f/+}$). We found that starting at 8-10 months of age, animals exhibited hunchback posture (kyphosis), weight loss, reduced reproduction, higher pro-inflammatory TNFa and IL-6 cytokines, infiltrating cells in lung and spleen, increased age-related p16, p21, p53, and CDK4 expression (Fig. 4G-J, Fig. S5B, S5C). Intriguingly, the front and hind limb grip strength of TFAM Het mice was less than that of the controls (Fig. 4K). Our open field analysis demonstrates that TFAM Het animals spent significantly less time in overall activity, gross mobility, and exploratory behavior than control mice (Fig. 4L). Intriguingly, the weight of TFAM Het mice at 8-10 months of age exhibited comparable (1.2-fold) changes to age- and sex-matched control $TFAM^{f/f}$ littermate mice (Fig. S5D). These findings suggest that intact TFAM in Tregs confers favorable and protective benefits against negative alterations caused by decreasing TFAM expression in old age, which have been linked to age-related cognitive and behavioral impairment (Fig. 4M).

**Discussion**

In conclusion, our findings show the critical involvement of mitochondrial TFAM in Tregs activity and regulate the mediated cellular and transcriptional dynamics to shape $CD4^+$ T cell subsets. Loss of mitochondrial protein has been linked with age-related pathologies[34-36], although knowledge of their role in maintaining $CD4^+$ T cell immune diversity is limited.

Numerous studies from both mice and humans have shown that genetic changes resulting in defective Foxp3 expression ($Foxp3^{sf}$) reduce Treg numbers and suppressive function, leading to fatal autoimmunity[37,38]. To our surprise, TFAM ablation in Foxp3 T cells resulted in an increase in peripheral Tregs, as well as effector memory T cells, and a reduction in naive T cells. Notably, the rise of peripheral $CD4^+$ Tregs has been shown in aging mouse and human model[7,12]. Although, an increase in Tregs may be relevant if older Tregs remain suppressive activity. While, in our model, TFAM ablation of Tregs leads in Tregs with distinct inflammatory surface markers and regulons, decreased $CD4^+$ T cell suppressive activity, and an enriched $CD4^+CD44^{hi}CD62L^{lo}$ effector T cell population. However, it remains unclear if aging's thymic involution transforms naive T cells into Tregs. The animal studies showing no difference between thymic and peripheral Tregs numbers, indicates putative surge in $CD4^+$ T cells becoming Treg in aging, although conventional techniques offer limited evidence[39]. Given that TFAM depletion causes increased oxidative stress and decreased cellular efficiency with age[16], we believe that removing TFAM from Tregs compromises $CD4^+$ T cell subset diversity and regulated functions. Indeed, Treg TFAM deficiency leads to dynamic changes in cell differentiation, resulting in the enrichment of inflammatory pathogenic aTreg, effector T memory, and cytotoxic cells, raising systemic inflammation and heightening pathways of Parkinson's, ALS, and Alzheimer's disease, as well as reducing lifespan.

Interestingly, the increased and impaired suppressive Tregs from TFAM cKO overall exacerbated inflammatory responses, unlike other Treg dysfunctional model[40-43]. Notably, TFAM cKO animals display a significant rise in the enrichment of age-related pathways and markers, as well as an increase in frailty and catastrophic reductions in health and function. Because TFAM cKO mice have a limited lifetime, assessing cognitive and physical impairments in old age is challenging. TFAM-Het mice (expressing 50% TFAM compared to TFAM cKO) display physiological and cognitive deficits as early as 8 months of age with comparable weight changes to control mice, expanding the potential value of the TFAM Het mouse model in researching age-related inflammatory pathologies. While human aging leads in organ atrophy and weight loss, 24-36-month mice with a 2- to 3-fold greater body weight than young control mice are not a suitable physiological model for the development of human therapeutics for pharmaceutical, pathogenesis, or vaccination purposes.

Taken together, our findings imply that TFAM modulates $Foxp3^+$ Treg suppressive activity and that TFAM might be a therapeutic target for inflammatory or aging-related diseases. The TFAM Het mouse model that allows for in-depth research on mechanisms driving degenerative diseases.

## Methods

**Animals.** $Foxp3^{YFPCre}$ (Stock No: 016959) and $TFAM^{f/f}$ (Stock No: 026123) mice were obtained from Jackson Laboratory (Bar Harbor, ME) and bred at the UND animal facility to create $Foxp3^{Cre}TFAM^{f/f}$. All mice used in this study were from C57BL/6 backgrounds. Animals were kept and bred in the UND Animal facility in a pathogen-free unit with a 12-hour light cycle, temperature, and humidity control. Efforts are being made to reduce animal suffering and needless usage, in accordance with the Institutional Animal Care and Use Committee's (IACUC) and National Institutes of Health's Guide for the Care and Use of Laboratory Animals standards.

**Histology, immunohistochemistry, and acquisition of images.** Formalin-fixed, paraffin-embedded slices of various tissues were deparaffinized on slides using xylene twice for 5 minutes each. Following that, they were switched to 100% ethanol twice for 3 minutes each and then to 95%, 75%, 65%, 50%, 35%, and 25% ethanol for 3 minutes each. Rinse the slides for ten minutes under running tap water. The excess water was removed using a wiper (KIMTECH SCIENCE) and 10% fetal bovine serum (FBS) in PBS was applied to the sections of the slides and incubated for 30 minutes in the dark at room temperature (RT). FBS was gently drained from the slides and cleaned with PBS (1X). MitoSpy (excitation (ex)/emission (em) at 577nm/598nm, MitoSpyTM Red CMXros (Cat# 424801, BioLegend). After incubation, slides were washed twice with 1X PBS and a single drop of mounting media (Fluoromount-G™ with DAPI, Cat# 00-4958-02, Thermo Fisher Scientific) was applied to the tissue sections and the coverslip was dipped into the mounting solution. The fluorescence images were collected using a Leica Thunder Imaging system and Olympus TIF Fluorescence microscope. Histology image scanned by Hamamatsu nanozoomer at UND histology core.

**Western blot.** Proteins were isolated from mouse tissue and/or single cells and homogenized in RIPA lysis buffer containing a 1% protease inhibitor cocktail[44-46]. The protein concentration was determined according to the manufacturer's instructions and our previously published protocol using the Bio-Rad protein assay reagent.

SDS-PAGE was used to extract a set quantity of cellular protein and electroblotted onto an Immobilon-P transfer membrane (cat# IPVH00010). The immunological blot was blocked for 1 hour at room temperature with 5% nonfat dry milk in TBST (25 mM Tris-HCL, pH 7.4, 1.5 M NaCl, 0.05% Tween-20), followed by overnight incubation with primary antibodies at 4 °C. The next day, the membranes were washed five times at six-minute intervals and incubated for one hour with HRP-conjugated secondary antibody (A16172, Invitrogen) (1:1000) in 3% nonfat dry milk in TBST. The blots were then washed five further times with TBST and developed with enhanced chemiluminescence. The following primary antibodies were bought from Cell Signaling Technologies (Cell Signaling Technology, MA 01923, USA): RIP (D94C12) Rabbit mAb #3493, MLKL (D2I6N) Rabbit monoclonal antibody #14993, RIPK3 (E1Z1D) Rabbit monoclonal antibody #13526, p-RIP (D1L3S) Rabbit monoclonal antibody #65746, p-MLKL Rabbit monoclonal antibody (D6H3V) #91689, p-RIP3(D6W2T) Rabbit monoclonal antibody #93654, p21 Waf1/Cip1 (12D1) rabbit monoclonal antibody #37543, p53 (1C12) Mouse monoclonal antibody #2524, CDK4 (D9G3E) Rabbit monoclonal antibody #12790, PCNA (D3H8P) XP® Rabbit monoclonal antibody #13110, p16 INK4A (D3W8G) GAPDH (D16H11) XP® Rabbit mAb #5174.

**RNA isolation and qPCR.** Total RNA was isolated from mouse tissues or single cells. The tissues were minced with a scissor and added to 500 µL of TRIzol reagent (Ambion, cat# 15596018, Life Technologies, USA)[44-46]. A Fisher Scientific Sonic Dismembrator 100 was used to fully homogenize tissue solutions (American Laboratory Trading, East Lyme, CT 06333. USA). The upper layer was removed, and the RNA was precipitated with an equivalent volume of isopropanol and incubated at 55°C for 10 minutes before being resuspended in 50 µL of RNase-free water (Promega, Madison, WI, USA). We determined the concentrations of RNA using a Smart-Spec plus spectrophotometer (Bio-Rad). Then, using a High-Capacity cDNA Reverse Transcription Kit (Cat#: 4368814, Applied Biosystem, Thermo Fisher Scientific), cDNA was generated from 0.5-1 µg of total RNA in a total volume of 25 µL. The RT-PCR program was run for 5 minutes at 25 °C, 30 minutes at 42 °C, and 30 minutes at 95 °C. The cDNA templates were further diluted in water two-three times. For qPCR, two microliters of diluted templates were utilized. A 96-well PCR plate (Cat#: MLL9601, Bio-Rad) was used for the qPCR. All genes were amplified twice, and each sample was analyzed in triplicate using 2X SYBR Green PCR mix (Cat#: B21202, Bimake.com) (Supplemental Table 6). After normalization to *Gapdh*, the CT value was utilized to compute the fold change in RNA abundance. qPCR reactions were performed using the Aria Mx Real-Time PCR equipment (Agilent).

**Flow cytometry and cytokine analysis.** Single-cell suspensions were prepared from mouse spleen. To assess $CD4^+$ T cell activation, we stained single-cell suspensions cell surface staining in 50µL FACS buffer (1% BSA, 2 mM EDTA, and 0.1% sodium azide in PBS, pH 7.4) (5-10x$10^5$ cells/tube) and incubated with antibodies for 30 minutes at 37°C. (106 cells/50 mL) with anti-CD45 PercpCy5.5 (Cat# 103132, Clone#30F11, BioLegend), anti-CD4 PE (Cat#100408, Clone#GK3.5, BioLegend), anti-CD44 Alexflour700 (Cat#103026,IM7, BioLegend), and anti-CD62L PeCy7 (Cat#104418, Clone# MEL/4, BioLegend) on ice for 30 minutes (Supplemental Table 6). Stained cells were then washed twice with 500µL of ice-cold FACS buffer to eliminate binding antibodies before being analyzed immediately using a BD FACSymphony A3Flow Cytometer. Annexin V APC staining cells were incubated with Annexin V APC (Cat#640920, BioLegend) for 3 minutes in the ice-cold FACS buffer and then washed. Followed by Propidium Iodide (Cat#6421301, BioLegend) added right before analyzing the cells by FACS. MitoSpy (Cat# 424801, BioLegend) staining was carried out in accordance with the manufacturer's recommendations. Cells were resuspended in MitoSpy in 300-400 µL of warm 1X PBS and incubated at 37 °C for 30 minutes. Cells were then washed twice with 1X PBS before being analyzed using a BD FACSymphony A3 Flow Cytometer on stained and unstained samples (BD Biosciences). For inflammatory cytokines detection, sera were collected from mice blood and measured by the LEGENDplex mouse inflammation panel according to the manufacturer's instructions (Cat#740446, BioLegend). Samples were read on the BD FACSymphony Flow Cytometer.

**In vitro Treg suppression assay** Tregs ($CD4^+CD25^+$) cells were isolated from the spleen of sex-matched TFAM cKO and $TFAM^{f/f}$ (control) mice and Tconv ($CD4^+CD25^-$) from TFAM control mice using BD FACS ARIA™Ilu at the UND flowcytometry core: anti-CD4 PE (Cat#100408, Clone#GK3.5, BioLegend), anti-CD25 (Cat#102030, clone PC61, BioLegend). Afterward, 5x$10^4$ Tconv ($CD4^+CD25^-$) cells from TFAM control were labeled with CFSE Cell Division Tracker Kit (Cat# 423801, BioLegend) and cultured with mitomycin-treated wild type splenocytes. To detect Treg suppressive effect to these labeled Tconv ($CD4^+CD25^-$) cells culture, we added Tregs ($CD4^+CD25^+$) from the TFAM cKO and $TFAM^{f/f}$ (control) for 60 hours at 37°C with 2.5 µg/mL Dynabeads™ Mouse

T-Activator CD3/CD28 for T-Cell Expansion and Activation bead (Cat# 1145). After 60 hours, the CD4 cell proliferation was observed by FACS, and % suppression was calculated and displayed as indicated[46].

**Grip strength analysis.** Neuromuscular strength was assessed using the grip strength test. The forelimb and hindlimb grip strengths of mice were assessed by using a grip strength meter from San Diego Instruments. Each mouse was tested in three trials, and the force was recorded as grams-force (gf, 1 gf = 9.8 x $10^{-3}$ Newtons).

**Open field test.** Locomotor activity was measured in the open field test. A mouse was placed in the empty square cage from San Diego Instruments. Total distance (m) covered during a 10-min period was recorded and calculated by ANY-maze software (version 7.1).

**Cell isolation and sequencing library construction using the 10x Genomics Chromium platform**. Cells were isolated from spleens from WT and cKO mice by grinding with 70 µm cell strainers (Cat#22363548, Fisher brand). ACK RBC lysis buffer (Cat#A10492-01, Gibco) was used to lyse RBC. Trypan blue (Cat#25900CI, Corning) staining confirmed cell viability. The 10X Genomics Chromium system was used to create 3' single-cell gene expression libraries (v3.0) from WT and cKO spleen single-cell suspensions. On an Illumina HiSeq X Ten, pair-end 150 bp sequencing was used to generate high-quantity data (Illumina, San Diego, California, USA). Then, using Cell Ranger software v6.0.0, the output Illumina base call files from sequencing runs were combined and converted to FASTQ files using Illumina's bcl2fastq.

**Single-cell RNA-seq data alignment and sample aggregating**. RNA reads from the 10X Chromium platform with sequence quality less than 30 were filtered out and then mapped to the mm10 mouse reference genome using the CellRanger software (v6.0.0). Seurat (v4.0.2) was used to read the individual sample output files from CellRanger Count[47]. Cells were further filtered out of the downstream analysis using the following criteria: *nFeature RNA < 200 & nFeature RNA > 4000 & percent.mt >25*. Scrublet (v0.2.3)[48] was used to detect probable doublets and then *CellCycleScoring in Seurat was used* to define the cell cycle phase by using a published list of cell cycle genes[49]. *SCTransform* (v0.3.2) from Seurat was used to independently normalize the gene-cell count matrices with default parameters[50]. Dimension reductions, including principal component analysis (PCA), clustering, and t-distributed Stochastic Neighbor Embedding (t-SNE) projections (resolution=0.7) were then performed on the normalized data. By following a similar pipeline, subclusters for $CD4^+$ T cells were identified.

**Cell type annotation and differential expression analysis**. To determine the cell type of each cluster, the *FindAllMarkers* function in Seurat was used to find the cluster's gene markers. Cell types were allocated manually after consulting the CellMarker[51] and PanglaoDB[52] databases. MAST (v1.18.0)[53] was utilized to conduct differential analysis on each cell type to find the genes that were differentially expressed between WT and cKO cells with the adjusted p-value <0.05 and absolute log2FC >0.25. The Gene Set Enrichment Analysis (GSEA) for Kyoto Encyclopedia of Genes and Genomes (KEGG) was done using the richR package (https://github.com/hurlab/richR), with a p-value of 0.01 used as the cutoff value to identify significant KEGG pathways.

**Single-cell trajectory reconstruction for $CD4^+$ T cell**. The Monocle2 R package (v2.20.0, http://cole-trapnell-lab.github.io/monocle-release/) was used to reconstruct cell fate choices and pseudotime trajectories. The gene-cell matrix of UMI counts was sent to Monocle, which then created an object using its new Cell Data Set function (*lower Detection Limit = 0.5, expression Family = nonbinomial.size*). We evaluated the size factors and dispersion of gene expression. We next used the differentialGeneTest module to conduct differential expression analysis in order to determine the ordering of genes using the parameter "*fullModelFormulaStr = ~celltype*," and then maintained genes with q values less than 1E-3 for downstream analysis. Following the *setOrderingFilter* function, the *reduceDimension* module with the argument "*method = DDRTree*" was used to reduce the dimensionality of the data. When *orderCells* is executed, the root state variable may be adjusted to reflect the known biological background. Following that, the *plot_cell_trajectory* and *plot_pseudotime_heatmap* functions were used to visualize the data further.

**RNA velocity analysis**. Velocyto (v0.17.17) was used to analyze the velocity of RNA in cells[54]. This method utilizes the relative amount of unspliced and spliced mRNA as a predictor of future cell state. Annotation of spliced and unspliced reads was conducted using the Python script velocyto.py in the Cell Ranger output folder utilizing the Velocyto pipeline. Then, the scvelo (v0.2.3)[55] was used to determine the $CD4^+$ T cell velocity. The

previously normalized data served as the basis for calculating first and then order moments for each cell in relation to its closest neighbors (*scvelo.pp.moments(n pcs = 30, n neighbors = 30)*). Following that, the velocities were calculated, and the velocity graph was produced using the *scvelo.tl.velocity* and *scvelo.tl.velocity* graph functions with the mode set to 'stochastic'. Finally, using the *scvelo.tl.velocity* embedding function, the velocity field was projected onto the existing t-SNE coordinates.

**Transcription factor regulons prediction.** Gene regulatory network (GRN) was generated using pyscenic package (v0.11.0)[56]. Briefly, the raw expression matrix for the cells of all samples was filtered by keeping genes with a total expression greater than 3*0.01*(number of cell). Then the *pyscenic.grn* command was used with *grnboost2* method and default options and a fixed seed to derive co-expression modules between transcription factors and potential targets. The following database: cisTarget databases (*mm10__refseq-r80__10kb_up_and_down_tss.mc9nr.feather, mm10__refseq-r80__500bp_up_and_100bp_down_tss.mc9nr. feather*), the transcription factor motif annotation database (*motifs-v9-nr.mgi-m0.001-o0.0.tbl*) and the list of mouse transcription factors (*mm_mgi_tfs.txt*) were downloaded for the analysis. A regulon is a group of target genes regulated by a common transcription factor. AUCell (Area Under the Curve) scores (regulon activities) in each cell were computed with *pycenic.aucell* command (default parameters). These scores were then binarized into either “on” or “off” states, by setting an optimized threshold on the distribution of each regulon among all cells using the *skimage.filters.threshold_minimum* function.

**Bulk RNA-seq data processing**. Low Quality (Q<30) and sequencing adapters were removed with Trimmomatic software v0.36[57] from raw reads. Clean reads were then mapped to the mouse reference genome (mm10) by using HISAT2[58]. FeatureCounts[59] were used to summarize the unique mapped reads to mouse genes. Differential gene expression analysis was performed using DESeq2[60] with adjusted p-value < 0.05 and fold change >2 as the cutoff for identifying differentially expressed genes (DEGs). Gene Set Enrichment Analysis (GSEA) on KEGG pathway data was performed by using the richR package and the adjusted p-value < 0.05 was chosen as the cutoff value to select significant KEGG pathways.

**Acknowledgments**
We thank the Bony De Kumar, Epigenetic core, Steve Anderson and Subha Nookala, Flow cytometry core, Neeta Adhikari and Donna Laturnus Histology core, Sarah Abrahamson Imaging core, Ellen Olson, Dr Collin Combs, Behavior Research Core, Computational Data Analysis core at the University of North Dakota.

**Funding:** UND NIH Epigenetic COBRE Pilot Grant for Single cell RNA seq data to S.J. UND NIH Host-Pathogen Interactions COBRE Pilot Grant**,** grant (grant no. NIGMS/NIH-P20GM1034442) to R.M. Histological services provided by the UND Histology Core Facility are supported by NIH/NIGMS awards P20GM113123, U54GM128729, and UND SMHS funds. UND Imaging core provide help to imaging and supported by NIH grant P20GM113123, DaCCOTA CTR NIH grant U54GM128729, and UNDSMHS funds, Mouse Behavior services provided by the UND Behavior Research Core Facility are supported by NIH/NIGMS awards P20GM103442. ND INBRE (P20GM103442) will provide support in part for related supplies, travel, software, and technical personnel. Computational Data Analysis core was supported by NIH/NIGMS award P20GM113123. EA supported by Eva Gilbertson, M.D. foundation Study grant to JD.

**Author contributions:** R.M. conceived and designed the study, K.G, R.M. and Z.W. analyzed and interpreted the scRNA-seq and RNA-seq data, T.D., Z.W., H.M., A.L. and S.J. performed the experiments. R.M., K.G., N.K. and Z.W. organized the figures and wrote the manuscript. R.M., K.G., N.K., J.H., Z.W., D.J., H.B., M.G. and A.T. revised the manuscript. All authors provided comments on the manuscript.

**Competing interests:** The authors declare no competing interests.

**Data and materials availability**: All data associated with this study are present in the paper or the Supplementary Materials.

**Figure Legends:**

**Figure 1: TFAM in Foxp3$^{+}$ Tregs role as a determinant of CD4-lineage distribution and to regulate immune-mediated aging.**

**A.** Schematic representation of the single cell RNA sequencing (scRNA-seq).

**B.** t-SNE projection of 49,156 cells with 21 cell types (Erythroid cells were removed) were obtained from Foxp3$^{Cre}$Tfam$^{f/f}$ (cKO: 14,198) and controlled splenocyte Tfam$^{f/f}$ (WT: 34,958). Color stand for different cell type.

**C.** t-SNE projection of all 7,821 cells (WT: 4,324; cKO: 3,497) of CD4$^{+}$ T cells presenting six different CD4$^{+}$ T cells (Naïve, TEM, Exhausted, nTregs, aTregs and Cytotoxic cells). Color stand for different cell types.

**D.** Track plot showing gene expression profile (rows) across cells (columns). Track height represents gene expression. Each bar represents a gene expression signal from a single cell.

**E.** Relative changes of six types of CD4$^{+}$ T cell between cKO and WT.

**F.** GSEA for KEGG pathways for CD4$^{+}$ T cells between cKO and WT. Color stands for the up-regulated (red) or down-regulated (blue) in cKO.

**G.** Pseudotime map of the CD4$^{+}$ T cells reflects the developing relationships and reveals potential paths of the CD4$^{+}$ T subtypes in WT and cKO. Each dot represents one cell and color stands for different cell type.

**H.** Velocities derived from the dynamical model for CD4$^{+}$ T cells are visualized as streamlines in a t-SNE-based embedding.

**I.** Expression patterns of the the genes in four clusters. Columns represent cells ordered by pseudotime, while rows represent genes were grouped based on similarity in gene expression. Genes in clusters 1 are expressed early in pseudotime, and genes in cluster 2 are expressed late. KEGG enrichment analyses were performed for genes in each cluster, with selected significantly enriched pathways shown.

**J.** CD4$^{+}$CD44$^{hi}$CD62L$^{lo}$ CD4 effector and CD4$^{+}$CD44$^{lo}$CD62L$^{hi}$ CD4 naïve T cell from WT and cKO mice detected by FACS, and **K.** mean fluorescence intensity (MFI) plot from different organs. CD4$^{+}$ T effector T cell number greatly increased in spleen and lymph node (LN) of the cKO mice compared to the WT mice.

**L.** T cell suppression assay for labeled CD4$^{+}$ Tconv cells co-cultured with Tregs in indicated ratio for 60 hours in the presence of CD3/CD28 stimulated or non-stimulated Tconv cell proliferation detected by FACS Symphony, data analyzed by FlowJo, plotted as percent suppression.

Data represented as mean ± SD. Statistical test used: two-way ANOVA with post-hoc test (K, L).

**Figure 2: TFAM ablation exhibits systemic pathology and accelerates immune aging in Foxp3$^{Cre}$Tfam$^{f/f}$ mice.**

**A.** Representative photograph from cKO mouse (right) exhibits deteriorated appearance compared to the same age (8 weeks) and sex littermate WT mouse (left).

**B.** Increased spleen and lymph node size in cKO mouse compared to WT mouse.

**C.** cKO mouse (right) shows increased spine curvature compared to the same age (8 weeks) and sex littermate WT mouse (left) (Representative X Ray image).

**D.** Kaplan-Meier survival curve for WT (n=10; M/F) and cKO mice (n=10, M/F).

**E.** Histology sections stained by H&E from bone, muscle and skin and images were taken by light microscope, and **F.** quantification of muscle and bone density plotted.

**G.** Serum cytokines of TNF$\alpha$ and IL-6 were detected by Legend plex, and calculated values plotted.

**H.** H&E and Mitospy staining in spleen section form cKO mouse compared to WT mouse.

**I.** Mitospy staining from WT and cKO splenocytes, detected by FACS and plotted as a histogram.

**J.** p16 and p21 aging marker from mouse spleen detected by quantitative PCR and plotted.

**K.** Protein expression of aging markers including CDK4, PCNA, p53, p21, p16, LC3B and GAPDH detected by western blot.

**L.** Differential expression genes expression profiling between WT and cKO in the spleen.

**M.** Bulk RNA-seq expression data from cKO mice compared to the WT mice showed reduced protein and N-Glycan biosynthesis pathways in spleen, reduced circadian rhythm in the skin, and increased neuroactive ligand-receptor signaling in the brain of cKO mice.

Data represented as mean ± SD. Statistical test used: WT (n=5-10; M/F) and cKO mice (n=5-10, M/F).

**Figure 3. Inflammatory and cell death pathways predominate in TFAM cKO mice**

**A.** Heatmap of all $CD4^+$ T cells showing the high-confidence regulons among WT and cKO mice. "On" indicates active regulons; "Off" indicates inactive regulons. Active regulons per cell appear in black; the horizontal color bar indicates the subset associated with each cell and group. Numbers in parentheses represent the number of genes comprising the regulon.
**B.** Dotplot shows the expression of *Prdm1*, *Nfkb1*, *Nfkb2* and *Ahr* between WT and cKO among all $CD4^+$ T cells.
**C.** Inflammatory *TNFα*, *IL-1β*, and *IL-6* cytokines expression detected by qPCR from WT and cKO spleen.
**D.** Heatmap showed the expression profiling of the genes involved in apoptosis and necroptosis between WT and cKO in the spleen.
**E.** Protein expression of cleaved caspase-3 and caspase-8, IκBα, TNF downstream pRIPK1/RIPK1, pRIPK3/RIPK3, pMLKL/MLKL and GAPDH as loading control detected by western blot.
**F.** Annexin V staining for live and dead cells from spleen and skin detected by flow cytometry in WT and cKO mice.
**G.** GSEA for KEGG pathways for monocyte, macrophage, and dendritic cells (DC) between cKO and WT. Color stands for the up-regulated (red) or down-regulated (blue) in cKO spleen.
Data represented as mean ± SD. Statistical test used: t-test, WT (n=5-10; M/F) and cKO mice (n=5-10, M/F).

**Figure 4. The restoration of TFAM function results to alleviate inflammation and aging pathologies.**
**A.** Schematics for oral treatment with resveratrol (RSV, 7 mg/kg QOD) or vehicle for cKO mice from weeks 4 to 8. QOD, every other day.
**B.** Skin histology stained for H&E and Mitospy from vehicle and resveratrol treated cKO mice.
**C.** TNFα and IL-6 serum cytokines from TFAM cKO mice.
**D.** Proinflammatory *TNFα*, *IL-6* and *IL-1β* cytokine expression detected by qPCR from vehicle and resveratrol treated cKO mice.
**E.** p16 and p21 expression were detected by western blot, and **F.** qPCR from vehicle and resveratrol treated cKO mice.
**G.** Representative photograph from TFAM Het ($Foxp3^{Cre}Tfam^{f/+}$, bottom) mouse showing exhibits aging appearance compared to the same age (8 months) and sex littermate control $Tfam^{f/f}$ mouse (top).
**H.** Old control mouse (WT, > 2 years old, top) and TFAM Het mouse (8 months, middle) shows increased spine curvature compared to the control $Tfam^{f/f}$ mouse (WT, 8 months, bottom) (Representative X Ray images).
**I.** Protein expression of aging markers including p16, p21, and GAPDH detected by western blot.
**J.** TNFα and IL-6 cytokine detected from serum from 8 weeks and 8 months of WT and cKO mice.
**K-L** Performance on behavior tests by 8 weeks and 8 months of TFAM Het ($Foxp3^{Cre}Tfam^{f/+}$) mice (n = 5-8) and WT mice (n = 6). **K.** Grip strength test showing the strength of forelimbs and hindlimbs between 8 weeks and 8 months of TFAM Het and WT mice. **L.** Representative tracing graphs (left) and quantification of the total distance (m, right) in 10 min during the open field test.
**M.** Representative working model.
Data represented as mean ± SD. Statistical test used: t-test (C, D, F), two-way ANOVA with post-hoc test (J, K, L). WT (n=5-10; M/F) and cKO mice (n=5-10, M/F).

**Supplementary Figure 1. Landscape of scRNA-seq analysis of WT and cKO spleen.**
**A.** t-SNE projections of single-cell transcriptomes from WT and cKO mice before Erythroid cells were removed, annotated by cell type. Each dot denotes a distinct cell.
**B.** Cell subset proportions (top) and numbers (bottom) for WT and cKO spleens.
**C.** Dot plot of mean expression of canonical marker genes for 20 major lineages from tissues of each origin, as indicated.
**D.** Gene Set Enrichment Analysis (GSEA) of KEGG pathways for all cell types between cKO and WT (Only age-related pathways are selected). Color stands for the up-regulated (red) or down-regulated (blue) in cKO spleen. Enriched terms were identified as significant at a p-value ≤ 0.01.
**E.** Expression of aged-related genes (*Fcer2a*, *Cd79b*, *Zfp36l2*, and *S100a6*) on Figure 1B t-SNE embedding. Each dot corresponds to a single cell.

**Supplementary Figure 2. scRNA-seq results show the cellular heterogeneity in $CD4^+$ T cells.**
**A.** Relative proportion of $CD4^+$ T cells among WT and cKO spleen, color stands for cell type.
**B.** Violin plot showing the expression profile of age-related genes among all $CD4^+$ T cells.
**C.** Monocle 2 prediction of $CD4^+$ T cell subsets developmental trajectory with pseudotime. Each dot represents an individual cell.

**D.** Monocle 2 trajectory cell states for all $CD4^+$ T cells, each branch represents one cell state (left). Barplots representing cell proportions in the seven states of WT and cKO (right). Cells are colored according to seven states, which partition the trajectory.
**E.** Relative proportion of $CD4^+$ T cells among different states of WT and cKO spleen, color stands for cell type.
**F.** Functional enrichment analysis of KEGG pathways with up-regulated differential expressed genes for the cell states. Only top 20 of the enriched pathways were plotted from each state.

**Supplementary Figure 3. Increased cell infiltration and inflammation in different organs in $Foxp3^{Cre}Tfam^{f/f}$ mice.**
**A.** Histology sections stained with H&E from lung, liver, colon, and kidney.
**B.** Serum cytokines identified by Legend plex for IL-1β, IL-10, MCP1, IL-23, IL-1α, IL-17, IFNγ, IL-12, IFNβ, GM-CSF, and IL-27 with estimated values displayed.
Data represented as mean ± SD. Statistical test used: t-test, WT (n=5-10; M/F) and cKO mice (n=5-10, M/F).

**Supplementary Figure 4. t-SNE projection of binary regulon activity of *Irf8*, *Runx2*, *Bcl11a*, and *Nfkb1*.**

**Supplementary Figure 5. Restoration of mitochondrial function leads to mitigate pathologies.**
**A.** H&E histology section for lung, liver, and kidney for RSV treated WT and cKO mice.
**B.** Representative images of H&E histology in spleen and lung from WT (8 weeks, 8 months, and 3 years) and Het (8 weeks and 8 months) mice.
**C-D.** Body weight (**C**) and fold change (**D**) of young and old WT and cKO mice.
Data represented as mean ± SD. Statistical test used: two-way ANOVA with post-hoc test (C). WT (n=5; M/F) and Het mice (n=5, M/F).

**Supplemental Table 1. Gene Set Enrichment Analysis (GSEA) of KEGG pathway between cKO and WT for all cell types.**

**Supplemental Table 2. Gene Set Enrichment Analysis (GSEA) of KEGG pathway between cKO and WT for CD4 subsets.**

**Supplemental Table 3. Functional enrichment analysis of KEGG pathway for four clusters.**

**Supplemental Table 4. Functional enrichment analysis of KEGG pathway for Monocle states.**

**Supplemental Table 5. Gene Set Enrichment Analysis (GSEA) of KEGG pathway between cKO and WT from Brain, Spleen and Skin RNA-seq.**

**Supplemental Table 6. Primer sequences for RT-qPCR, antibodies for Western blots and flow cytometry, and other reagents.**

**References**


1. Goronzy, J.J. & Weyand, C.M. Successful and Maladaptive T Cell Aging. *Immunity* **46**, 364-378 (2017).
2. Suo, C.*, et al.* Mapping the developing human immune system across organs. *Science*, eabo0510 (2022).
3. Fontenot, J.D., Gavin, M.A. & Rudensky, A.Y. Foxp3 programs the development and function of CD4+CD25+ regulatory T cells. *Nat Immunol* **4**, 330-336 (2003).
4. Hori, S., Nomura, T. & Sakaguchi, S. Control of regulatory T cell development by the transcription factor Foxp3. *Science* **299**, 1057-1061 (2003).
5. Oliveira, G.*, et al.* Landscape of helper and regulatory antitumour CD4(+) T cells in melanoma. *Nature* **605**, 532-538 (2022).
6. Elyahu, Y.*, et al.* Aging promotes reorganization of the CD4 T cell landscape toward extreme regulatory and effector phenotypes. *Sci Adv* **5**, eaaw8330 (2019).
7. Oldenhove, G.*, et al.* Decrease of Foxp3+ Treg cell number and acquisition of effector cell phenotype during lethal infection. *Immunity* **31**, 772-786 (2009).
8. Grinberg-Bleyer, Y.*, et al.* NF-kappaB c-Rel Is Crucial for the Regulatory T Cell Immune Checkpoint in Cancer. *Cell* **170**, 1096-1108 e1013 (2017).
9. Sakaguchi, S.*, et al.* Regulatory T Cells and Human Disease. *Annu Rev Immunol* **38**, 541-566 (2020).
10. DiSpirito, J.R.*, et al.* Molecular diversification of regulatory T cells in nonlymphoid tissues. *Sci Immunol* **3**(2018).
11. Lages, C.S.*, et al.* Functional regulatory T cells accumulate in aged hosts and promote chronic infectious disease reactivation. *J Immunol* **181**, 1835-1848 (2008).
12. Chiu, B.C., Stolberg, V.R., Zhang, H. & Chensue, S.W. Increased Foxp3(+) Treg cell activity reduces dendritic cell co-stimulatory molecule expression in aged mice. *Mech Ageing Dev* **128**, 618-627 (2007).
13. Guo, Z.*, et al.* DCAF1 regulates Treg senescence via the ROS axis during immunological aging. *J Clin Invest* **130**, 5893-5908 (2020).
14. Li, J.*, et al.* A conserved NAD(+) binding pocket that regulates protein-protein interactions during aging. *Science* **355**, 1312-1317 (2017).
15. Sun, N., Youle, R.J. & Finkel, T. The Mitochondrial Basis of Aging. *Mol Cell* **61**, 654-666 (2016).
16. Desdin-Mico, G.*, et al.* T cells with dysfunctional mitochondria induce multimorbidity and premature senescence. *Science* **368**, 1371-1376 (2020).
17. Weinberg, S.E.*, et al.* Mitochondrial complex III is essential for suppressive function of regulatory T cells. *Nature* **565**, 495-499 (2019).
18. Chapman, N.M.*, et al.* mTOR coordinates transcriptional programs and mitochondrial metabolism of activated Treg subsets to protect tissue homeostasis. *Nat Commun* **9**, 2095 (2018).
19. Fu, Z.*, et al.* Requirement of Mitochondrial Transcription Factor A in Tissue-Resident Regulatory T Cell Maintenance and Function. *Cell Rep* **28**, 159-171 e154 (2019).
20. Awasthi, A., Murugaiyan, G. & Kuchroo, V.K. Interplay between effector Th17 and regulatory T cells. *J Clin Immunol* **28**, 660-670 (2008).
21. Beriou, G.*, et al.* IL-17-producing human peripheral regulatory T cells retain suppressive function. *Blood* **113**, 4240-4249 (2009).
22. Hovhannisyan, Z., Treatman, J., Littman, D.R. & Mayer, L. Characterization of interleukin-17-producing regulatory T cells in inflamed intestinal mucosa from patients with inflammatory bowel diseases. *Gastroenterology* **140**, 957-965 (2011).
23. Overacre-Delgoffe, A.E.*, et al.* Interferon-gamma Drives Treg Fragility to Promote Anti-tumor Immunity. *Cell* **169**, 1130-1141 e1111 (2017).
24. Oh, H.*, et al.* An NF-kappaB Transcription-Factor-Dependent Lineage-Specific Transcriptional Program Promotes Regulatory T Cell Identity and Function. *Immunity* **47**, 450-465 e455 (2017).
25. van der Veeken, J.*, et al.* The Transcription Factor Foxp3 Shapes Regulatory T Cell Identity by Tuning the Activity of trans-Acting Intermediaries. *Immunity* **53**, 971-984 e975 (2020).
26. Pasparakis, M. & Vandenabeele, P. Necroptosis and its role in inflammation. *Nature* **517**, 311-320 (2015).
27. Bernardi, P., Scorrano, L., Colonna, R., Petronilli, V. & Di Lisa, F. Mitochondria and cell death. Mechanistic aspects and methodological issues. *Eur J Biochem* **264**, 687-701 (1999).
28. Lee, S., Park, K., Kim, J., Min, H. & Seong, R.H. Foxp3 expression in induced regulatory T cells is stabilized by C/EBP in inflammatory environments. *EMBO Rep* **19**(2018).
29. Jurivich, D.A.*, et al.* Human aging alters the first phase of the molecular response to stress in T-cells. *Exp Gerontol* **40**, 948-958 (2005).

30. Maj, T.*, et al.* Oxidative stress controls regulatory T cell apoptosis and suppressor activity and PD-L1-blockade resistance in tumor. *Nat Immunol* **18**, 1332-1341 (2017).
31. Brown-Borg, H.M., Borg, K.E., Meliska, C.J. & Bartke, A. Dwarf mice and the ageing process. *Nature* **384**, 33 (1996).
32. Lagouge, M.*, et al.* Resveratrol improves mitochondrial function and protects against metabolic disease by activating SIRT1 and PGC-1alpha. *Cell* **127**, 1109-1122 (2006).
33. Verdura, S.*, et al.* Resveratrol targets PD-L1 glycosylation and dimerization to enhance antitumor T-cell immunity. *Aging (Albany NY)* **12**, 8-34 (2020).
34. Misrani, A., Tabassum, S. & Yang, L. Mitochondrial Dysfunction and Oxidative Stress in Alzheimer's Disease. *Front Aging Neurosci* **13**, 617588 (2021).
35. Merlini, E., Coleman, M.P. & Loreto, A. Mitochondrial dysfunction as a trigger of programmed axon death. *Trends Neurosci* **45**, 53-63 (2022).
36. Wiley, C.D.*, et al.* Mitochondrial Dysfunction Induces Senescence with a Distinct Secretory Phenotype. *Cell Metab* **23**, 303-314 (2016).
37. Sakaguchi, S. Naturally arising Foxp3-expressing CD25+CD4+ regulatory T cells in immunological tolerance to self and non-self. *Nat Immunol* **6**, 345-352 (2005).
38. Chang, X.*, et al.* The Scurfy mutation of FoxP3 in the thymus stroma leads to defective thymopoiesis. *J Exp Med* **202**, 1141-1151 (2005).
39. Chougnet, C.A.*, et al.* A major role for Bim in regulatory T cell homeostasis. *J Immunol* **186**, 156-163 (2011).
40. Sasaki, K.*, et al.* Modulation of autoimmune pathogenesis by T cell-triggered inflammatory cell death. *Nat Commun* **10**, 3878 (2019).
41. Saravia, J.*, et al.* Homeostasis and transitional activation of regulatory T cells require c-Myc. *Sci Adv* **6**, eaaw6443 (2020).
42. O'Hagan, K.L., Miller, S.D. & Phee, H. Pak2 is essential for the function of Foxp3+ regulatory T cells through maintaining a suppressive Treg phenotype. *Sci Rep* **7**, 17097 (2017).
43. Grinberg-Bleyer, Y.*, et al.* The Alternative NF-kappaB Pathway in Regulatory T Cell Homeostasis and Suppressive Function. *J Immunol* **200**, 2362-2371 (2018).
44. Mathur, R.*, et al.* A mouse model of Salmonella typhi infection. *Cell* **151**, 590-602 (2012).
45. Mathur, R.*, et al.* Induction of autophagy in Cx3cr1(+) mononuclear cells limits IL-23/IL-22 axis-mediated intestinal fibrosis. *Mucosal Immunol* **12**, 612-623 (2019).
46. Park, S.G.*, et al.* T regulatory cells maintain intestinal homeostasis by suppressing gammadelta T cells. *Immunity* **33**, 791-803 (2010).
47. Stuart, T.*, et al.* Comprehensive Integration of Single-Cell Data. *Cell* **177**, 1888-1902 e1821 (2019).
48. Wolock, S.L., Lopez, R. & Klein, A.M. Scrublet: Computational Identification of Cell Doublets in Single-Cell Transcriptomic Data. *Cell Syst* **8**, 281-291 e289 (2019).
49. Kowalczyk, M.S.*, et al.* Single-cell RNA-seq reveals changes in cell cycle and differentiation programs upon aging of hematopoietic stem cells. *Genome Res* **25**, 1860-1872 (2015).
50. Hafemeister, C. & Satija, R. Normalization and variance stabilization of single-cell RNA-seq data using regularized negative binomial regression. *Genome Biol* **20**, 296 (2019).
51. Zhang, X.*, et al.* CellMarker: a manually curated resource of cell markers in human and mouse. *Nucleic Acids Res* **47**, D721-d728 (2019).
52. Franzén, O., Gan, L.M. & Björkegren, J.L.M. PanglaoDB: a web server for exploration of mouse and human single-cell RNA sequencing data. *Database (Oxford)* **2019**(2019).
53. Finak, G.*, et al.* MAST: a flexible statistical framework for assessing transcriptional changes and characterizing heterogeneity in single-cell RNA sequencing data. *Genome Biol* **16**, 278 (2015).
54. La Manno, G.*, et al.* RNA velocity of single cells. *Nature* **560**, 494-498 (2018).
55. Bergen, V., Lange, M., Peidli, S., Wolf, F.A. & Theis, F.J. Generalizing RNA velocity to transient cell states through dynamical modeling. *Nat Biotechnol* **38**, 1408-1414 (2020).
56. Van de Sande, B.*, et al.* A scalable SCENIC workflow for single-cell gene regulatory network analysis. *Nat Protoc* **15**, 2247-2276 (2020).
57. Bolger, A.M., Lohse, M. & Usadel, B. Trimmomatic: a flexible trimmer for Illumina sequence data. *Bioinformatics* **30**, 2114-2120 (2014).
58. Kim, D., Langmead, B. & Salzberg, S.L. HISAT: a fast spliced aligner with low memory requirements. *Nat Methods* **12**, 357-360 (2015).

59. Liao, Y., Smyth, G.K. & Shi, W. featureCounts: an efficient general purpose program for assigning sequence reads to genomic features. *Bioinformatics* **30**, 923-930 (2014).
60. Love, M.I., Huber, W. & Anders, S. Moderated estimation of fold change and dispersion for RNA-seq data with DESeq2. *Genome Biol* **15**, 550 (2014).

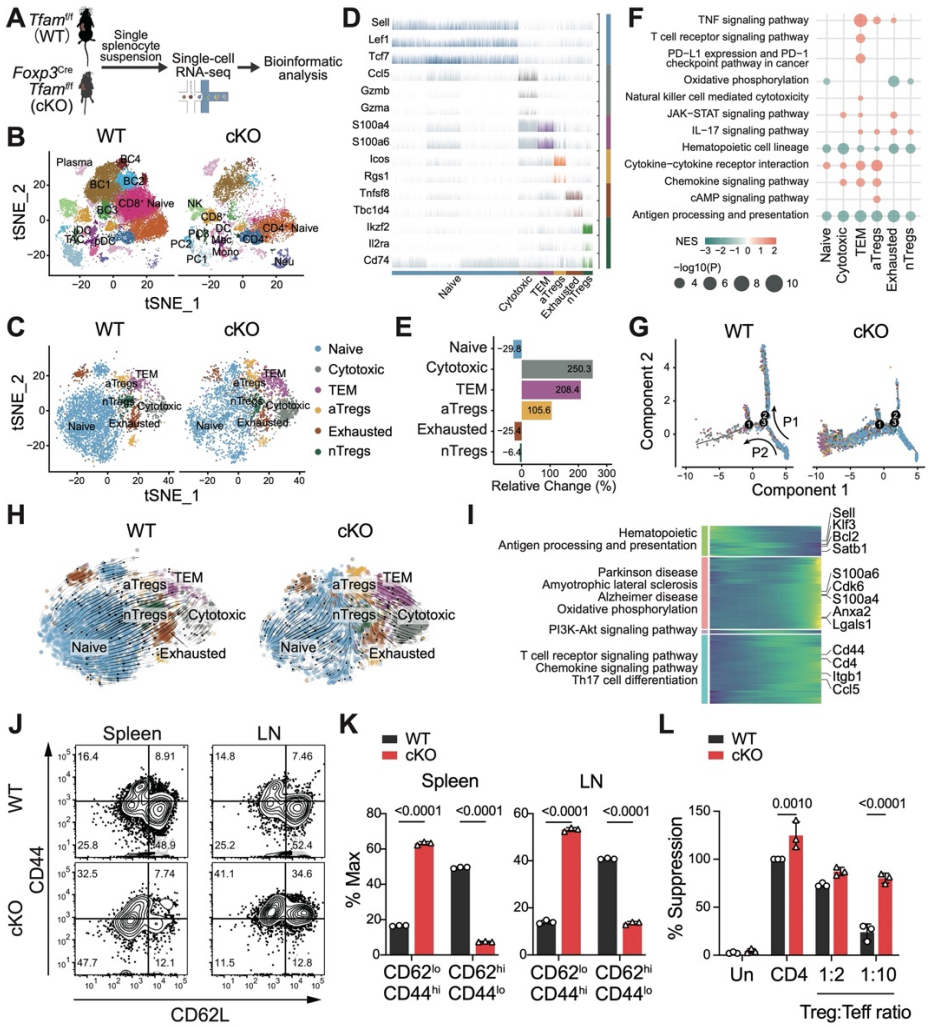


**Figure 1: TFAM in Foxp3⁺ Tregs role as a determinant of CD4-lineage distribution and to regulate immune-mediated aging.**

**A.** Schematic representation of the single cell RNA sequencing (scRNA-seq). **B.** t-SNE projection of 49,156 cells with 21 cell types (Erythroid cells were removed) were obtained from Foxp3$^{Cre}$Tfam$^{f/f}$ (cKO: 14,198) and controlled splenocyte Tfam$^{f/f}$ (WT: 34,958). Color stand for different cell type. **C.** t-SNE projection of all 7,821 cells (WT: 4,324; cKO: 3,497) of CD4$^+$ T cells presenting six different CD4$^+$ T cells (Naïve, TEM, Exhausted, nTregs, aTregs and Cytotoxic cells). Color stand for different cell types. **D.** Track plot showing gene expression profile (rows) across cells (columns). Track height represents gene expression. Each bar represents a gene expression signal from a single cell. **E.** Relative changes of six types of CD4$^+$ T cell between cKO and WT. **F.** GSEA for KEGG pathways for CD4$^+$ T cells between cKO and WT. Color stands for the up-regulated (red) or down-regulated (blue) in cKO. **G.** Pseudotime map of the CD4$^+$ T cells reflects the developing relationships and reveals potential paths of the CD4$^+$ T subtypes in WT and cKO. Each dot represents one cell and color stands for different cell type. **H.** Velocities derived from the dynamical model for CD4$^+$ T cells are visualized as streamlines in a t-SNE-based embedding. **I.** Expression patterns of the the genes in four clusters. Columns represent cells ordered by pseudotime, while rows represent genes were grouped based on similarity in gene expression. Genes in clusters 1 are expressed early in pseudotime, and genes in cluster 2 are expressed late. KEGG enrichment analyses were performed for genes in each cluster, with selected significantly enriched pathways shown. **J.** CD4$^+$CD44$^{hi}$CD62L$^{lo}$ CD4 effector and CD4$^+$CD44$^{lo}$CD62L$^{hi}$ CD4 naïve T cell from WT and cKO mice detected by FACS, and **K.** mean fluorescence intensity (MFI) plot from different organs. CD4$^+$ T effector T cell number greatly increased in spleen and lymph node (LN) of the cKO mice compared to the WT mice. **L.** T cell suppression assay for labeled CD4$^+$ Tconv cells co-cultured with Tregs in indicated ratio for 60 hours in the presence of CD3/CD28 stimulated or non-stimulated Tconv cell proliferation detected by FACS Symphony, data analyzed by FlowJo, plotted as percent suppression. Data represented as mean ± SD. Statistical test used: two-way ANOVA with post-hoc test (K, L).

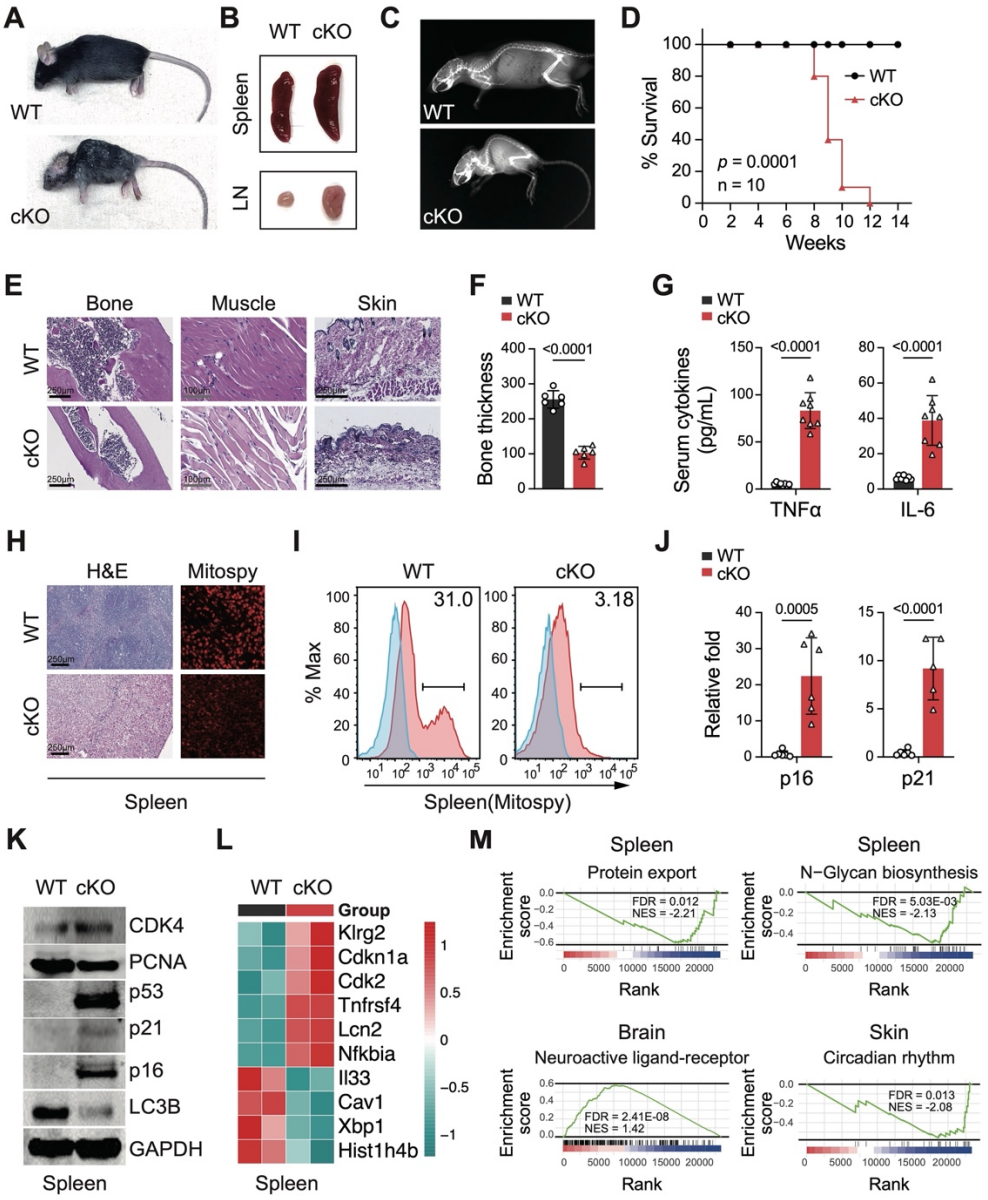


**Figure 2: TFAM ablation exhibits systemic pathology and accelerates immune aging in Foxp3$^{Cre}$Tfam$^{f/f}$ mice.** **A.** Representative photograph from cKO mouse (right) exhibits deteriorated appearance compared to the same age (8 weeks) and sex littermate WT mouse (left). **B.** Increased spleen and lymph node size in cKO mouse compared to WT mouse. **C.** cKO mouse (right) shows increased spine curvature compared to the same age (8 weeks) and sex littermate WT mouse (left) (Representative X Ray image). **D.** Kaplan-Meier survival curve for WT (n=10; M/F) and cKO mice (n=10, M/F). **E.** Histology sections stained by H&E from bone, muscle and skin and images were taken by light microscope, and **F.** quantification of muscle and bone density plotted. **G.** Serum cytokines of TNF$\alpha$ and IL-6 were detected by Legend plex, and calculated values plotted. **H.** H&E and Mitospy staining in spleen section form cKO mouse compared to WT mouse. **I.** Mitospy staining from WT and cKO splenocytes, detected by FACS and plotted as a histogram. **J.** p16 and p21 aging marker from mouse spleen detected by quantitative PCR and plotted. **K.** Protein expression of aging markers including CDK4, PCNA, p53, p21, p16, LC3B and GAPDH detected by western blot. **L.** Differential expression genes expression profiling between WT and cKO in the spleen. **M.** Bulk RNA-seq expression data from cKO mice compared to the WT mice showed reduced protein and N-Glycan biosynthesis pathways in spleen, reduced circadian rhythm in the skin, and increased neuroactive ligand-receptor signaling in the brain of cKO mice. Data represented as mean ± SD. Statistical test used: WT (n=5-10; M/F) and cKO mice (n=5-10, M/F).

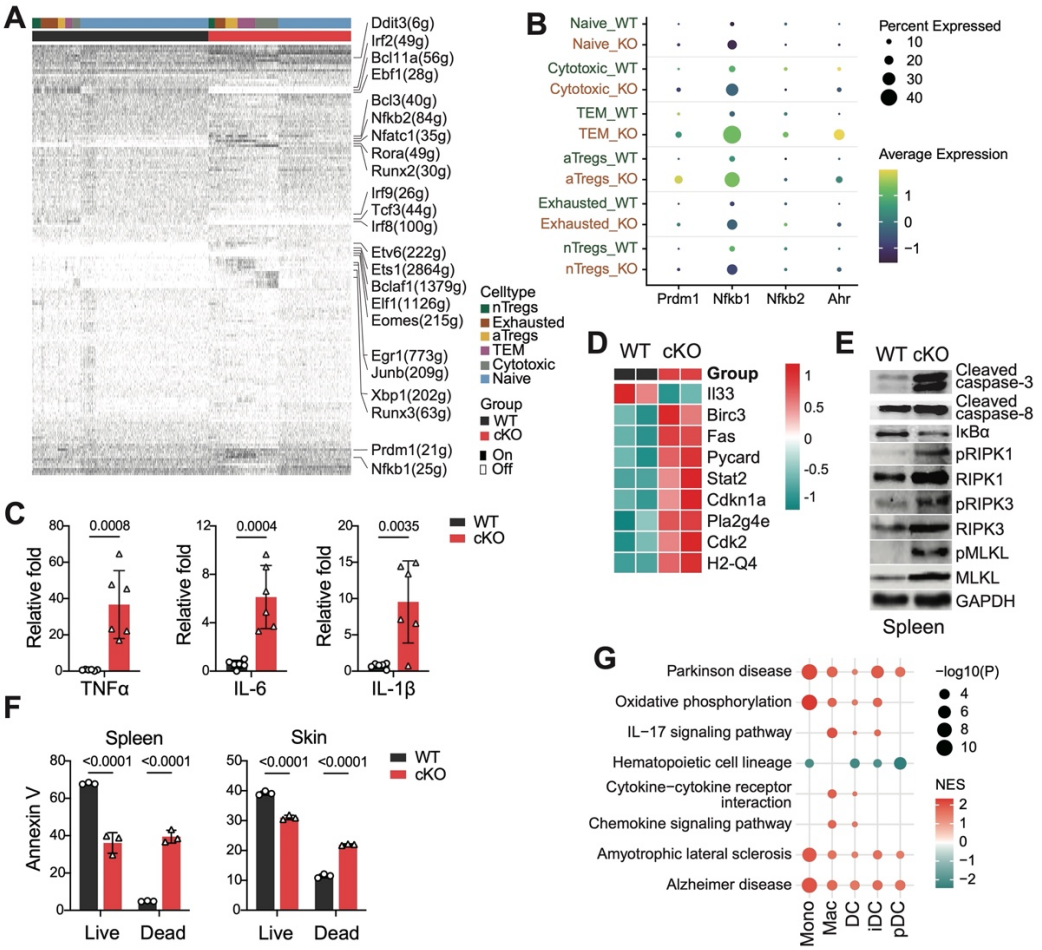


**Figure 3. Inflammatory and cell death pathways predominate in TFAM cKO mice**

**A.** Heatmap of all CD4$^+$ T cells showing the high-confidence regulons among WT and cKO mice. "On" indicates active regulons; "Off" indicates inactive regulons. Active regulons per cell appear in black; the horizontal color bar indicates the subset associated with each cell and group. Numbers in parentheses represent the number of genes comprising the regulon. **B.** Dotplot shows the expression of *Prdm1*, *Nfkb1*, *Nfkb2* and *Ahr* between WT and cKO among all CD4$^+$ T cells. **C.** Inflammatory *TNFα*, *IL-1β*, and *IL-6* cytokines expression detected by qPCR from WT and cKO spleen. **D.** Heatmap showed the expression profiling of the genes involved in apoptosis and necroptosis between WT and cKO in the spleen. **E.** Protein expression of cleaved caspase-3 and caspase-8, IκBα, TNF downstream pRIPK1/RIPK1, pRIPK3/RIPK3, pMLKL/MLKL and GAPDH as loading control detected by western blot. **F.** Annexin V staining for live and dead cells from spleen and skin detected by flow cytometry in WT and cKO mice. **G.** GSEA for KEGG pathways for monocyte, macrophage, and dendritic cells (DC) between cKO and WT. Color stands for the up-regulated (red) or down-regulated (blue) in cKO spleen. Data represented as mean ± SD. Statistical test used: t-test, WT (n=5-10; M/F) and cKO mice (n=5-10, M/F).

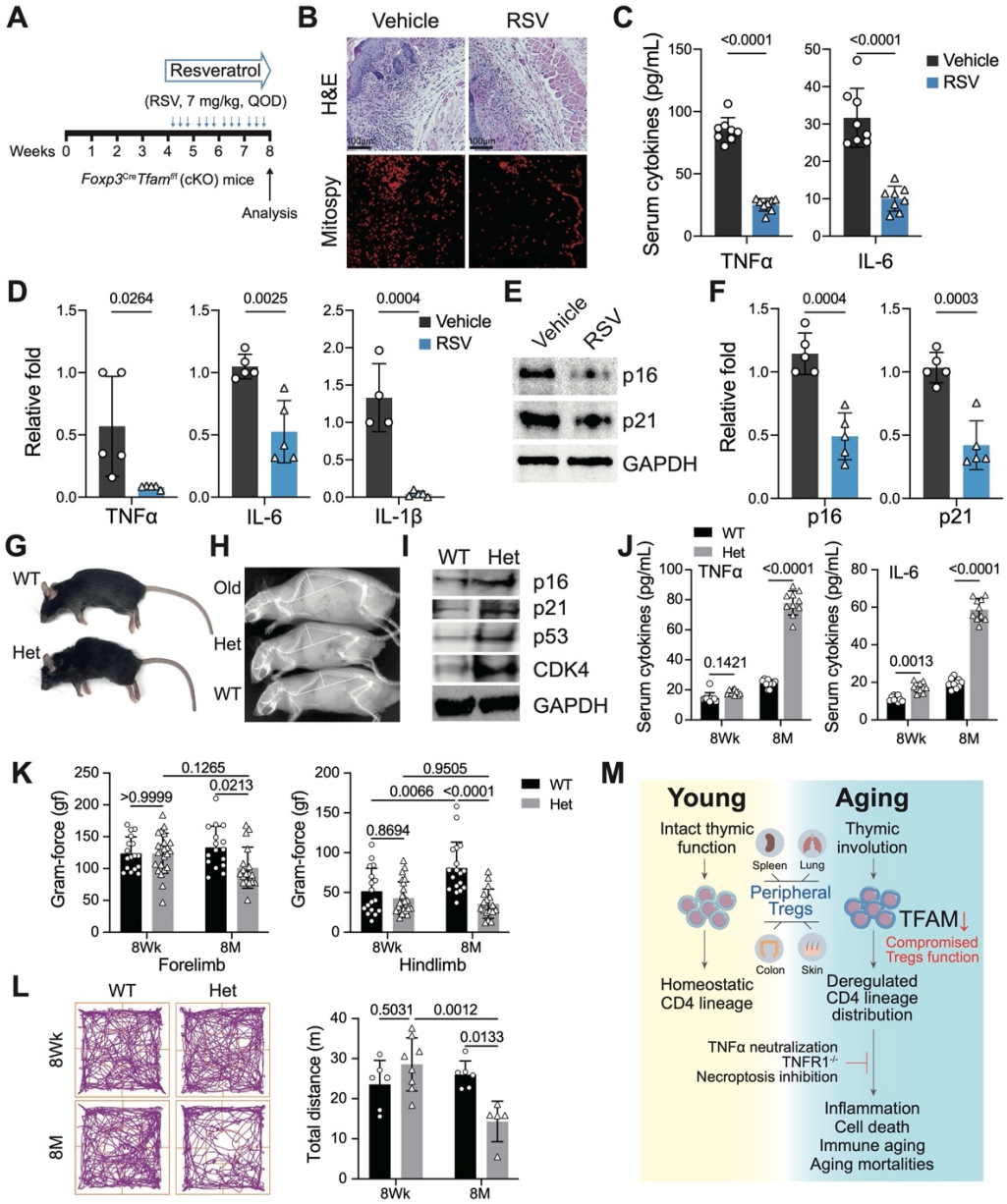


**Figure 4. The restoration of TFAM function results to alleviate inflammation and aging pathologies.**
**A.** Schematics for oral treatment with resveratrol (RSV, 7 mg/kg QOD) or vehicle for cKO mice from weeks 4 to 8. QOD, every other day. **B.** Skin histology stained for H&E and Mitospy from vehicle and resveratrol treated cKO mice. **C.** TNF$\alpha$ and IL-6 serum cytokines from TFAM cKO mice. **D.** Proinflammatory *TNF$\alpha$*, *IL-6* and *IL-1$\beta$* cytokine expression detected by qPCR from vehicle and resveratrol treated cKO mice. **E.** p16 and p21 expression were detected by western blot, and **F.** qPCR from vehicle and resveratrol treated cKO mice. **G.** Representative photograph from TFAM Het (Foxp3$^{Cre}$Tfam$^{f/+}$, bottom) mouse showing exhibits aging appearance compared to the same age (8 months) and sex littermate control Tfam$^{f/f}$ mouse (top). **H.** Old control mouse (WT, > 2 years old, top) and TFAM Het mouse (8 months, middle) shows increased spine curvature compared to the control Tfam$^{f/f}$ mouse (WT, 8 months, bottom) (Representative X Ray images). **I.** Protein expression of aging markers including p16, p21, and GAPDH detected by western blot. **J.** TNF$\alpha$ and IL-6 cytokine detected from serum from 8 weeks and 8 months of WT and cKO mice. **K-L** Performance on behavior tests by 8 weeks and 8 months of TFAM Het (Foxp3$^{Cre}$Tfam$^{f/+}$) mice (n = 5-8) and WT mice (n = 6). **K.** Grip strength test showing the strength of forelimbs and hindlimbs between 8 weeks and 8 months of TFAM Het and WT mice. **L.** Representative tracing graphs (left) and quantification of the total distance (m, right) in 10 min during the open field test. **M.** Representative working model. Data represented as mean ± SD. Statistical test used: t-test (C, D, F), two-way ANOVA with post-hoc test (J, K, L). WT (n=5-10; M/F) and cKO mice (n=5-10, M/F).

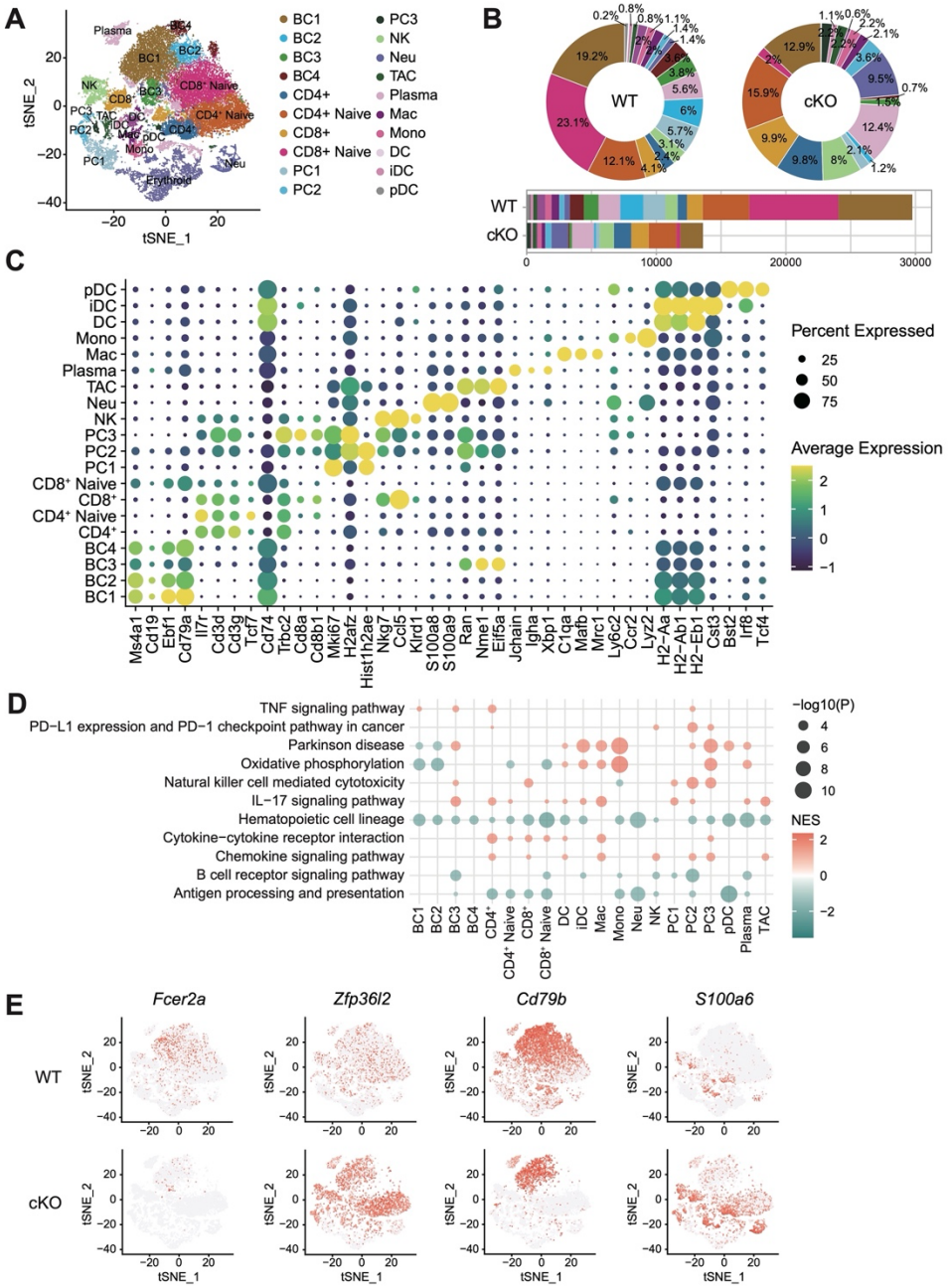


**Supplementary Figure 1. Landscape of scRNA-seq analysis of WT and cKO spleen.**
**A.** t-SNE projections of single-cell transcriptomes from WT and cKO mice before Erythroid cells were removed, annotated by cell type. Each dot denotes a distinct cell. **B.** Cell subset proportions (top) and numbers (bottom) for WT and cKO spleens. **C.** Dot plot of mean expression of canonical marker genes for 20 major lineages from tissues of each origin, as indicated. **D.** Gene Set Enrichment Analysis (GSEA) of KEGG pathways for all cell types between cKO and WT (Only age-related pathways are selected). Color stands for the up-regulated (red) or down-regulated (blue) in cKO spleen. Enriched terms were identified as significant at a p-value ≤ 0.01. **E.** Expression of aged-related genes (*Fcer2a*, *Cd79b*, *Zfp36l2*, and *S100a6*) on Figure 1B t-SNE embedding. Each dot corresponds to a single cell.

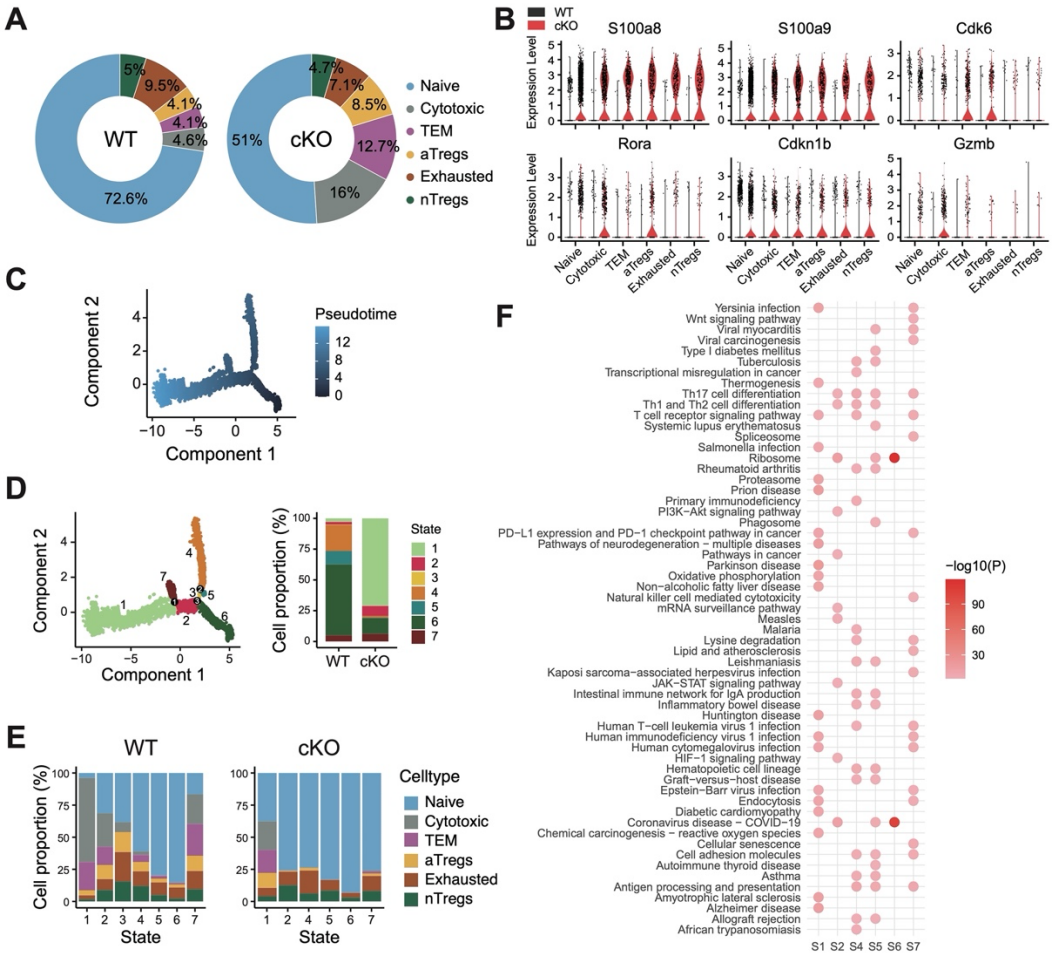


**Supplementary Figure 2. scRNA-seq results show the cellular heterogeneity in CD4⁺ T cells.**
**A.** Relative proportion of CD4⁺ T cells among WT and cKO spleen, color stands for cell type. **B.** Violin plot showing the expression profile of age-related genes among all CD4⁺ T cells. **C.** Monocle 2 prediction of CD4⁺ T cell subsets developmental trajectory with pseudotime. Each dot represents an individual cell. **D.** Monocle 2 trajectory cell states for all CD4⁺ T cells, each branch represents one cell state (left). Barplots representing cell proportions in the seven states of WT and cKO (right). Cells are colored according to seven states, which partition the trajectory. **E.** Relative proportion of CD4⁺ T cells among different states of WT and cKO spleen, color stands for cell type. **F.** Functional enrichment analysis of KEGG pathways with up-regulated differential expressed genes for the cell states. Only top 20 of the enriched pathways were plotted from each state.

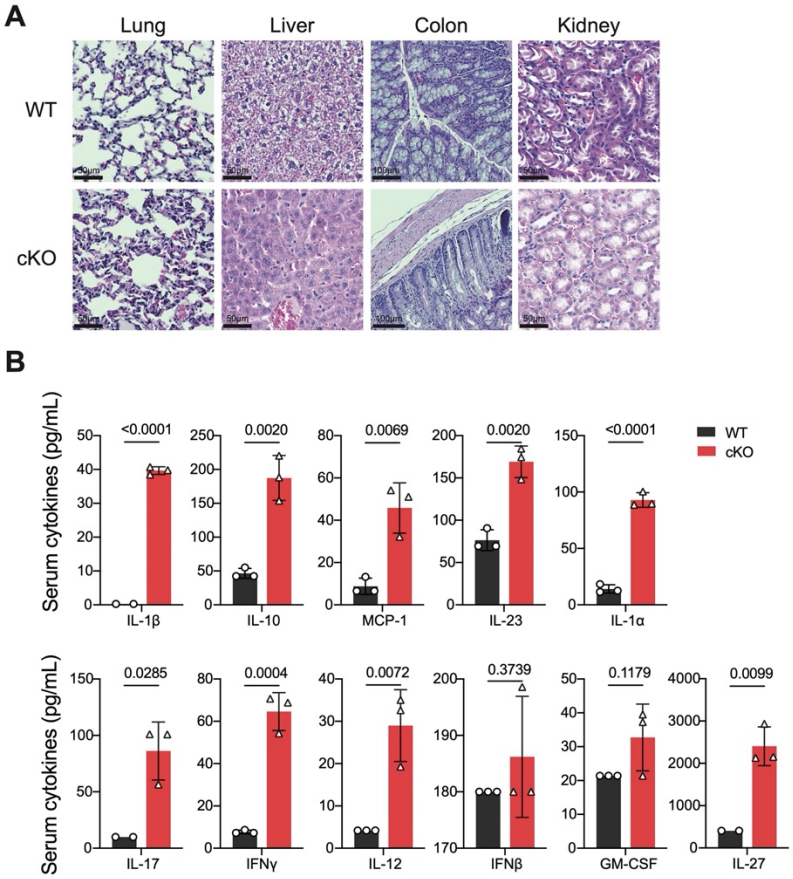


**Supplementary Figure 3. Increased cell infiltration and inflammation in different organs in Foxp3$^{Cre}$Tfam$^{f/f}$ mice.** **A.** Histology sections stained with H&E from lung, liver, colon, and kidney. **B.** Serum cytokines identified by Legend plex for IL-1β, IL-10, MCP1, IL-23, IL-1α, IL-17, IFNγ, IL-12, IFNβ, GM-CSF, and IL-27 with estimated values displayed. Data represented as mean ± SD. Statistical test used: t-test, WT (n=5-10; M/F) and cKO mice (n=5-10, M/F).

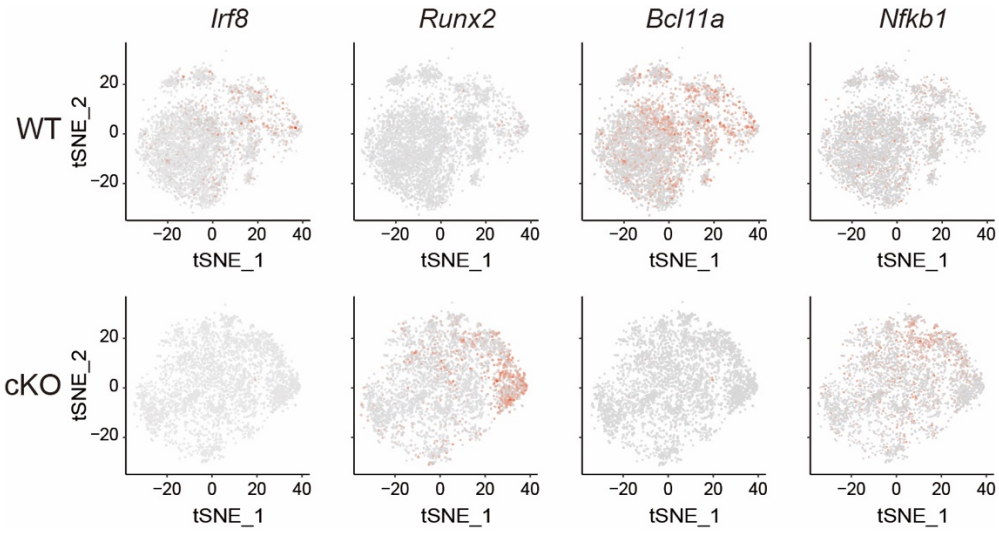


**Supplementary Figure 4. t-SNE projection of binary regulon activity of *Irf8*, *Runx2*, *Bcl11a*, and *Nfkb1*.**

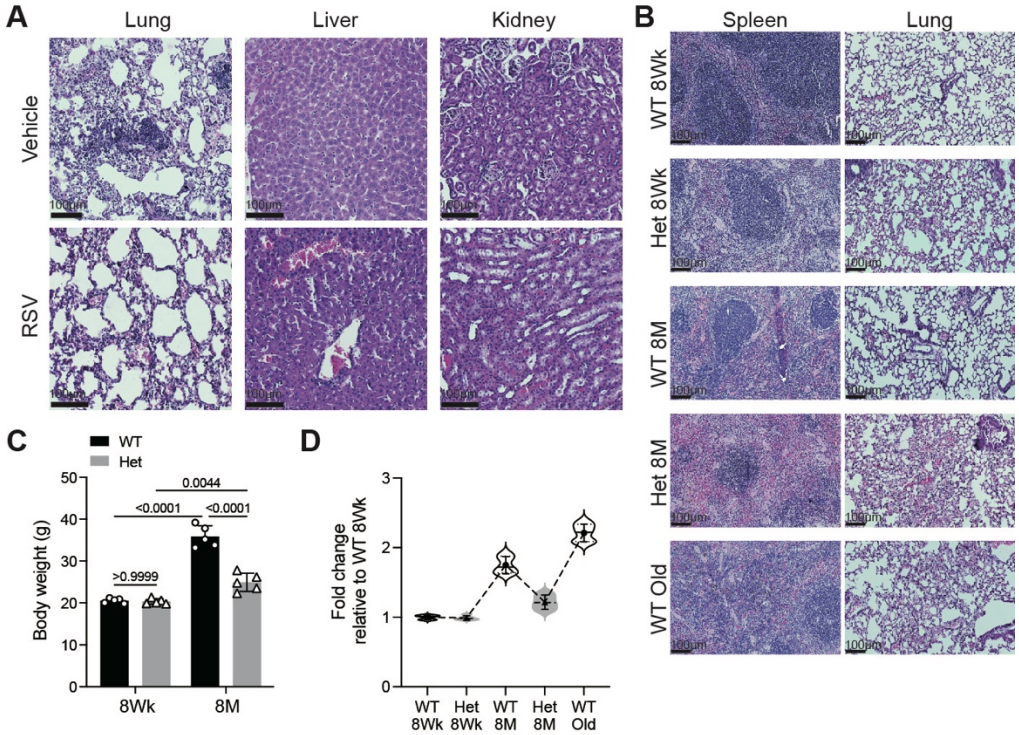


**Supplementary Figure 5. Restoration of mitochondrial function leads to mitigate pathologies.**
**A.** H&E histology section for lung, liver, and kidney for RSV treated WT and cKO mice. **B.** Representative images of H&E histology in spleen and liver from WT (8 weeks, 8 months, and 3 years) and Het (8 weeks and 8 months) mice. **C-D.** Body weight (**C**) and fold change (**D**) of young and old WT and cKO mice. Data represented as mean ± SD. Statistical test used: two-way ANOVA with post-hoc test (C). WT (n=5; M/F) and Het mice (n=5, M/F).

**Supplemental Table 1. Gene Set Enrichment Analysis (GSEA) of KEGG pathway between cKO and WT for all cell types.**

**Supplemental Table 2. Gene Set Enrichment Analysis (GSEA) of KEGG pathway between cKO and WT for CD4 subsets.**

**Supplemental Table 3. Functional enrichment analysis of KEGG pathway for four clusters.**

**Supplemental Table 4. Functional enrichment analysis of KEGG pathway for Monocle states.**

**Supplemental Table 5. Gene Set Enrichment Analysis (GSEA) of KEGG pathway between cKO and WT from Brain, Spleen and Skin RNA-seq.**

**Supplemental Table 6. Primer sequences for RT-qPCR, antibodies for Western blots and flow cytometry, and other reagents.**